

# Striking Seasonality in the Secular Warming of the Northern Continents: Structure and Mechanisms

SUMANT NIGAM, NATALIE P. THOMAS, AND ALFREDO RUIZ-BARRADAS

*Department of Atmospheric and Oceanic Science, University of Maryland, College Park, College Park, Maryland*

SCOTT J. WEAVER

*Environmental Defense Fund, Washington, D.C.*

(Manuscript received 21 October 2016, in final form 17 March 2017)

## ABSTRACT

The linear trend in twentieth-century surface air temperature (SAT)—a key secular warming signal—exhibits striking seasonal variations over Northern Hemisphere continents; SAT trends are pronounced in winter and spring but notably weaker in summer and fall. The SAT trends in historical twentieth-century climate simulations informing the Intergovernmental Panel for Climate Change's Fifth Assessment show varied (and often unrealistic) strength and structure, and markedly weaker seasonal variation. The large intra-ensemble spread of winter SAT trends in some historical simulations was surprising, especially in the context of century-long linear trends, with implications for the detection of the secular warming signal.

The striking seasonality of observed secular warming over northern continents warrants an explanation and the representation of related processes in climate models. Here, the seasonality of SAT trends over North America is shown to result from land surface–hydroclimate interactions and, to an extent, also from the secular change in low-level atmospheric circulation and related thermal advection. It is argued that the winter dormancy and summer vigor of the hydrologic cycle over middle- to high-latitude continents permit different responses to the additional incident radiative energy from increasing greenhouse gas concentrations.

The seasonal cycle of climate, despite its monotony, provides an expanded phase space for the exposition of the dynamical and thermodynamical processes generating secular warming, and an exceptional cost-effective opportunity for benchmarking climate projection models.

## 1. Introduction

Surface air temperature over the Northern Hemisphere continents has risen sharply in recent decades. Linear trends in the 1970-onward period in the CRU-TS3.23 near-surface air temperature data (Harris et al. 2014) are in excess of  $0.7^{\circ}\text{C decade}^{-1}$  over Alaska and the Pacific Northwest, western-central Canadian provinces, and the Great Plains, that is, more than 3 times the century-long trends in these regions. Ascertaining whether the substantially larger recent trends are indicative of accelerated secular change, multidecadal natural variability, or both is challenging (e.g., Hegerl et al. 1996; Thompson et al. 2009; Fyfe et al. 2010), especially in view of the short instrumental record of surface observations, the evolving state of climate models (a common investigative tool), and the potential interaction of these

components. The processes generating continental warming moreover remain to be understood (e.g., Compo and Sardeshmukh 2009; Lu and Cai 2009; Stine et al. 2009; Stine and Huybers 2012; Wallace et al. 2012).

Model-based estimates (and attribution) abound but exhibit substantial spread in the warming scenarios generated with observed and projected increase of greenhouse gases (Murphy et al. 2004; Meehl et al. 2007; Flato et al. 2013), in part due to varied treatment of convection, clouds, and aerosols, and the very limited opportunities for validation of the multidecadal-to-centennial scale projections. In short, the climate projection models are deprived of the routine evaluative feedback that has informed and vastly improved the weather forecast models (Bauer et al. 2015). While occasional simulation of paleoclimates and generation of decadal-scale predictions provide some evaluative feedback (Meehl et al. 2014), these efforts are often piecemeal and computationally burdensome.

---

*Corresponding author:* Sumant Nigam, nigam@umd.edu

DOI: 10.1175/JCLI-D-16-0757.1

© 2017 American Meteorological Society. For information regarding reuse of this content and general copyright information, consult the [AMS Copyright Policy](http://www.ametsoc.org/PUBSReuseLicenses) ([www.ametsoc.org/PUBSReuseLicenses](http://www.ametsoc.org/PUBSReuseLicenses)).

Would broadening the reporting and analysis of historical and projected climate change beyond the current *annual-mean* warming focus advance process-level understanding and improve climate models? The seasonal variation in secular warming, especially if substantial—as shown to be the case over the northern continents—provides the precious phase space for the exposition of the operative dynamical and thermodynamical processes. The markedly different seasonal circulation and hydroclimate states can elicit different responses from the same radiative forcing, yielding unique process-level insights into the generation of continental warming. The seasonally resolved warming projections likewise provide an exceptional opportunity for vetting climate models. The present analysis is motivated by this evaluative opportunity, which has remained largely untapped despite not requiring additional model integrations.

The exploitation of seasonal and hemispheric variations in generating an expanded climate phase space for testing hypotheses is, of course, not without precedence: Understanding and modeling of ocean–atmosphere interactions in the tropics, for example, was furthered by the analysis of the counterintuitive seasonal cycle in the eastern ocean basins (Philander and Chao 1991; Mitchell and Wallace 1992; Nigam and Chao 1996). Both seasonal and hemispheric differences advanced understanding of the Hadley circulation (Lindzen and Hou 1988; Oort and Yienger 1996; Dima and Wallace 2003) and provided clues on the mechanism for the summertime strengthening of the Northern Hemisphere sea level pressure anticyclones (Hoskins 1996; Nigam and Chan 2009).

The seasonality of secular warming has been noted in several observational analyses, all of which indicate the winter–spring SAT trends to be stronger than the summer–fall ones. The analyzed regions include the global domain (Balling et al. 1998; Kusunoki et al. 2009), the Northern Hemisphere (Wallace et al. 1995; Stine et al. 2009; Stine and Huybers 2012; Wallace et al. 2012; Robeson et al. 2014), the continental United States (Wang et al. 2009; Redmond and Abatzoglou 2014), the western United States (Abatzoglou and Redmond 2007), the Pacific Northwest (Mote 2003; Abatzoglou et al. 2014), and Alaska, Canada, and Mexico (Redmond and Abatzoglou 2014). The recent period (1979–2005) SAT trends, stratified by season in the Intergovernmental Panel on Climate Change (IPCC) Fourth Assessment Report (AR4; Trenberth et al. 2007; Fig. 3.10), also show two clear maxima: winter warming over North America and spring warming over north-central Asia.

The seasonality in secular warming has also been studied using climate simulation datasets: Lu and

Cai's (2009) analysis of the IPCC AR4 global warming simulations showed the clear-sky downward longwave radiation at the surface to be important for the larger winter warming signal in the polar region; Dwyer et al. (2012) analyzed the previous version of climate simulations (CMIP3) focusing largely on the Arctic where the stronger winter warming was ascribed to the increasing sea ice loss. Kusunoki et al. (2009) and Wang et al. (2009) used atmospheric models forced by historical sea surface temperatures (SSTs) and greenhouse gas concentrations to study the regional and seasonal distribution of secular warming, especially over North America, which was attributed to multidecadal SST variability in the Pacific and Atlantic basins.

Finally, it is worth noting that while the seasonally distinct climate base states can serve as a prism for viewing the processes generating secular warming, each of these states is associated with different levels of internal variability (or dynamical noise), leading to different signal detection thresholds. Stine et al. (2009) argue that although warming is stronger in winter, the winter SAT trends are less significant on account of the larger variance of monthly temperature in boreal winter.

The seasonal perspective has clearly been useful in advancing understanding of several climate variability features but it is yet to be exploited in providing insights on the origin of regional and seasonal variations of secular warming, especially the centennial trends over the northern continents. The present analysis is motivated by these possibilities. The datasets and analysis method are discussed in section 2. The seasonal trends in SAT in different analyses of related observations are displayed in section 3. The boreal winter and summer SAT trends in the twentieth-century historical simulations from five climate models used in the IPCC's Fifth Assessment Report (AR5) are shown and discussed in section 4, which also focuses on two geographical regions of notable surface warming for the quantitative comparison of observed and modeled trends. The intra-ensemble spread of winter near-surface air temperature trends is also examined in section 4 where standard deviation (SD) of the century-long (and even longer period) linear trends is displayed for one U.S. and one European model, along with the winter trends in each ensemble member of the U.S. model. The ensemble-mean to intraensemble SD (or signal to noise) ratio for the winter SAT trend for all five models is shown in appendix A. Two mechanisms for the striking seasonality in observed SAT trends are discussed in section 5: a new mechanism rooted in land surface–hydroclimate interactions in section 5a, and a dynamical mechanism based on thermal advection by the secular change in

circulation in [section 5b](#). Concluding remarks follow in [section 6](#).

## 2. Datasets and analysis method

### a. Datasets

#### 1) OBSERVED SURFACE AIR TEMPERATURE

Four different analyses of the observed near-surface air temperature (SAT) are used to characterize the seasonality of SAT trends.

The CRU-TS3.23 monthly analysis from the Climate Research Unit of the University of East Anglia ([Harris et al. 2014](#)) is available on a 0.5° continental grid for the January 1901–December 2014 period from [http://www.cru.uea.ac.uk/cru/data/hrg/cru\\_ts\\_3.23/](http://www.cru.uea.ac.uk/cru/data/hrg/cru_ts_3.23/). Trends in the near-surface mean temperature (SAT) are analyzed in the present study.

The CRUTEM4 analysis from the UK Met Office's Hadley Centre provides monthly near-surface air temperature anomalies relative to the 1961–90 baseline ([Jones et al. 2012](#)). It is available on the coarser 5.0° land–ocean grid for the January 1850–September 2015 period from <http://www.cru.uea.ac.uk/cru/data/temperature/#datdow>, with a fair amount of data missing through the middle part of the twentieth century.

Berkeley Earth's monthly analysis of surface temperature ([Rhode et al. 2013](#)) is available on a 1.0° land–ocean grid from 1850–2015 and can be downloaded at <http://berkeleyearth.org/data/>. Data are provided as anomalies relative to the 1951–80 climatology.

Finally, the NASA Goddard Institute for Space Studies (GISS) analysis of near-surface temperature ([Hansen et al. 2010](#)) is available on a 2.0° land–ocean grid for the January 1880–September 2015 period from <http://www.esrl.noaa.gov/psd/data/gridded/data.gistemp.html>. Monthly anomalies relative to the 1951–80 baseline are provided.

#### 2) OBSERVED CONTINENTAL PRECIPITATION

The Global Precipitation Climatology Centre (GPCC; [Becker et al. 2013](#)) provides a monthly analysis of precipitation from quality-controlled station gauge data. GPCC's full data reanalysis version 7 data, available on a 0.5° continental grid for the January 1901–December 2013 period, are used here (see <http://www.esrl.noaa.gov/psd/data/gridded/data.gpcc.html#detail>). From the several available analyses of continental precipitation (including CRU-TS3.23), the GPCC analysis was chosen because of the larger number of stations used in the development of this gridded product, especially relative to CRU-TS3.23 and the Global Historical Climatology Network (GHCN) stations (The Climate Data Guide; [NCAR 2014](#)).

#### 3) EVAPOTRANSPIRATION

Evaporation measurements are sparse and generally confined to subgrid-scale basins, such as U.S. Department of Agriculture watersheds, the Oklahoma Mesonet, and the Illinois Water Survey field sites. Sparse pan measurements of evaporation do exist but inferring terrestrial evapotranspiration from them is challenging (e.g., [Brutsaert 2006](#)). For these reasons, evapotranspiration is often diagnosed, residually, from the atmospheric water balance (e.g., [Rasmusson 1968](#); [Ruiz-Barradas and Nigam 2005](#)).

Evapotranspiration from the University of Delaware's Terrestrial Water Budget Data Archive (version 4.01; [Matsuura and Willmott 2015](#)) is analyzed. Monthly data on a 0.5° continental grid from [http://climate.geog.udel.edu/~climate/html\\_pages/Global2014/README.GlobalWbTs2014.html](http://climate.geog.udel.edu/~climate/html_pages/Global2014/README.GlobalWbTs2014.html) are available for the January 1900–December 2014 period. Evapotranspiration was diagnosed at the University of Delaware from the monthly water budget, which was estimated from the monthly-averaged temperature and precipitation fields following modification of the Thornthwaite water budget procedure ([Willmott et al. 1985](#)).

Evapotranspiration from Princeton University's global land surface hydrology simulations with the Variable Infiltration Capacity (VIC) land surface model is also analyzed ([Sheffield and Wood 2007](#); [Sheffield et al. 2006](#)). Monthly data on a 1° continental grid from an offline simulation are available at <http://hydrology.princeton.edu/data.lsm.php> for the January 1948–December 2000 period. Evapotranspiration was calculated using a Penman–Monteith formulation with adjustments to canopy conductance to account for environmental factors.

#### 4) HISTORICAL CLIMATE SIMULATIONS

Simulations of twentieth-century climate from climate system models forced by historical gas emissions, aerosol loadings, and solar activity are briefly referred to as historical climate simulations ([Taylor et al. 2012](#)). Historical simulations from five participant models in the IPCC's Fifth Assessment Report are analyzed in this study; the model details are in [Table 1](#). The model choice reflects representation from the major modeling centers of both United States and Europe, with the limited selection allowing closer examination of model performance.

Trends are ensemble-averaged for historical simulations. The averaging of century-long linear trends from the simulation ensemble of each model was, perhaps, not necessary as the observed trend—the simulation

TABLE 1. Details of the analyzed CMIP5 historical climate simulations. Trends in the 1902–2004 period are investigated. (Expansions of acronyms are available online at <http://www.ametsoc.org/PubsAcronymList>.)

Model name	Modeling center	Number of realizations (ensemble size)	Grid resolution (longitude × latitude)	Available time period
CCSM4	NCAR	6	1.25° × 0.942°	1850–2005
GFDL-CM3	NOAA GFDL	5	2.5° × 2.0°	1860–2004
HadCM3	UKMO	9	3.75° × 2.5°	1860–2005
HadGEM2-ES	UKMO	4	1.875° × 1.25°	1860–2005
MPI-ESM-LR	MPI	3	1.875° × 1.865°	1850–2005

target—is obtained from just one realization of nature. The averaging was nonetheless undertaken to preclude any model-generated ultra-low-frequency (centennial and longer time scale) variability from aliasing the twentieth-century trend.

### b. Analysis method

The Grid Analysis and Display System (GrADS) toolkit is used for most analyses. The linear trend is computed using the least squares fitting. Seasons are defined in a customary manner [e.g., boreal winter is defined as the average of December–February (DJF)]. Seasonal averages are constructed prior to the computation of linear trend. Although not commutative, reversing the order of operations has a negligible impact; for example, it leads to a trend difference of  $10^{-7}^{\circ}\text{C decade}^{-1}$  in the century-long seasonal SAT trend. In the analysis of historical simulations, the linear trend in each ensemble member is averaged to yield the ensemble-mean trend. Again, reversing this process (i.e., computing linear trend in the ensemble-mean) led to insignificant differences. A 9-point smoother (the `smth9` function in GrADS) is applied to most figures in order to minimize noise and highlight the large-scale spatial features of the seasonal trends. Geographical averages are computed using the `aave` function in GrADS, which calculates area-weighted averages. The seasonal SAT trend plotted for each region is the trend in the regionally averaged SAT.

#### 1) CALCULATING THERMAL ADVECTION TENDENCY

The dynamical contribution to the SAT trend is assessed by inferring the geostrophic wind trend ( $\mathbf{V}_{g\_trend}$  in units of  $\text{m s}^{-1} \text{decade}^{-1}$ ) from the gradients in sea level pressure (SLP). Advection of the climatological surface temperature ( $T_{\text{Clim}}$ ) by  $\mathbf{V}_{g\_trend}$  yields the thermal advection trend ( $\mathbf{V}_{g\_trend} \cdot \nabla T_{\text{Clim}}$ ) in units of  $^{\circ}\text{C s}^{-1} \text{decade}^{-1}$ . The resulting SAT trend ( $T_{t\_dyn}$ ) is estimated by balancing this thermal advection trend with Newtonian damping of temperature,  $\mathbf{V}_{g\_trend} \cdot \nabla T_{\text{Clim}} \approx -\gamma T_{t\_dyn}$ , where the right-hand side

represents thermal damping of lower tropospheric temperature by synoptic transients;  $\gamma$  is taken as  $(3 \text{ days})^{-1}$  following Lau (1979, Table I therein). The above two terms represent the dominant balance in the thermodynamic equation in the middle to high latitudes; ignoring diabatic heating (e.g., radiative forcing in context of secular warming) here is not problematic given the focus on diagnosis of just the dynamical contribution to warming. A similar strategy was used in analysis of the extreme 2013/14 North American winter where thermal advection by the North Pacific Oscillation–west Pacific teleconnection was implicated in the extreme cold (Baxter and Nigam 2015).

#### 2) STATISTICAL SIGNIFICANCE OF LINEAR TRENDS

The statistical significance of the fitted trends is estimated from the ratio of the slope and its standard error. Significance at the 95% level is evaluated from the Student's  $t$  distribution using an effective sample size computed from the lag-1 autocorrelation of the detrended time series, as in the adjusted standard error and adjusted degrees of freedom method (AdjSE + AdjDF) (Santer et al. 2000).

### 3. Seasonal trends in observed surface air temperature

Surface air temperature exhibits a warming trend over the northern continents. The warming is pronounced in boreal winter and spring (Fig. 1) when the statistically significant century-long trend exceeds  $0.2^{\circ}\text{C decade}^{-1}$  over continental regions extending from the Gobi Desert to central Siberian uplands in Asia, and from the northern Great Plains to the western-central Canadian provinces in North America. Interestingly, SAT trends are considerably weaker in boreal summer and fall, with the Asian continent devoid of any significant warming in summer and the North American continent in fall, leading to slight attenuation of seasonal SAT variability. A notable exception is the Middle East and Saharan Africa where the warming SAT trend is most impressive in boreal summer, amplifying the seasonal cycle (and

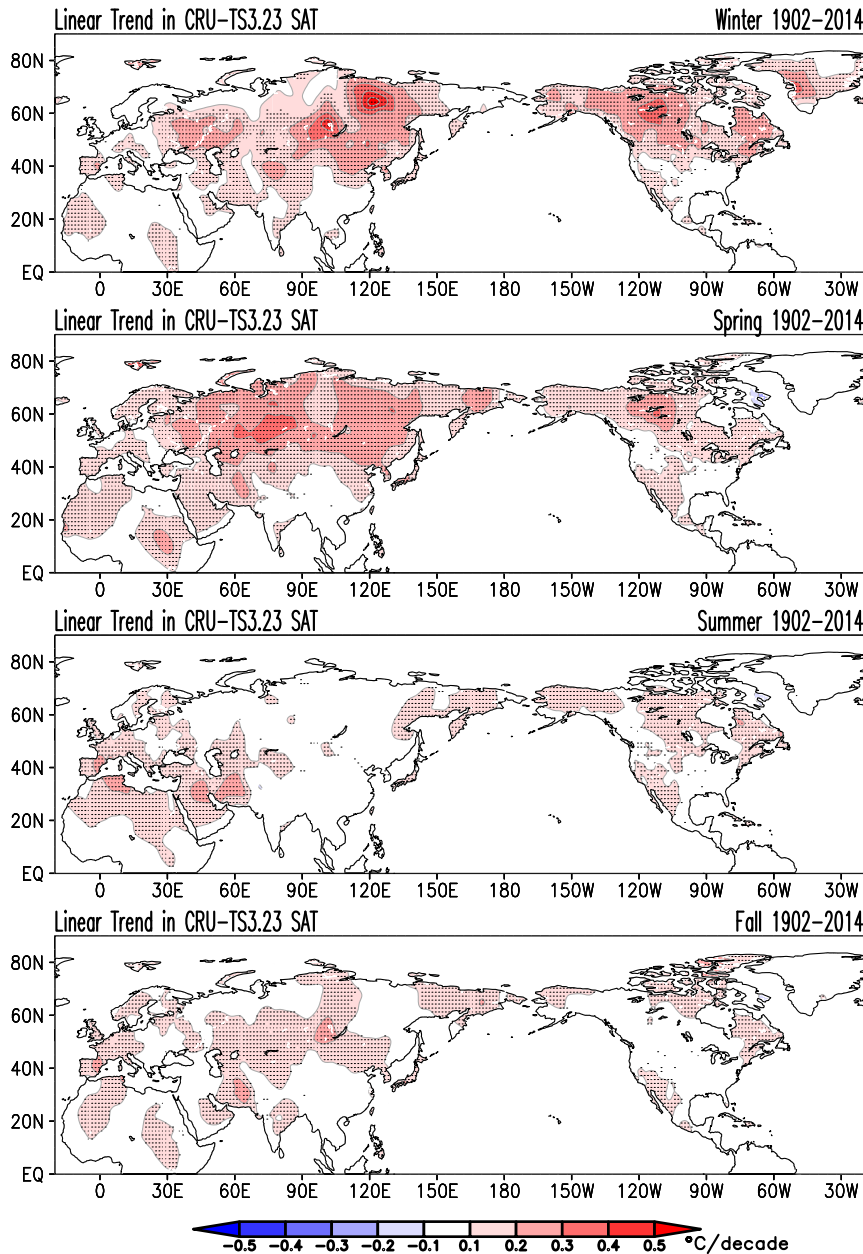


FIG. 1. The linear trend in *seasonal* near-surface air temperature (SAT) over the northern continents during 1902–2014. The 0.5° resolution CRU TS3.23 SAT is analyzed in boreal seasons: winter [December–February (DJF)], spring [March–May (MAM)], summer [June–August (JJA)], and fall [September–November (SON)]. Contour interval and shading threshold is 0.1°C decade<sup>-1</sup>, with warm colors showing a positive trend. The fields are shown after nine applications of the nine-point smoother (smth9) in GrADS. Trends significant at the 95% level are stippled.

heat-related stresses). Other noteworthy features in Fig. 1 include the following:

- the coherent subcontinental scale structure, with the winter–spring SAT trends neither longitudinally uniform nor latitudinally monotonic,
- the continental interior (and not Arctic rim) location of the maximum winter–spring SAT trends, and
- the weak trends (<|0.1|°C decade<sup>-1</sup>) over south central-eastern United States in all seasons.

The robustness of century-long SAT trends in the CRU-TS3.23 analysis is assessed by examining the corresponding trends in three independent analyses of SAT—CRUTEM4, Berkeley Earth, and NASA-GISS—in Fig. 2. Comparison of the winter trends (left column)

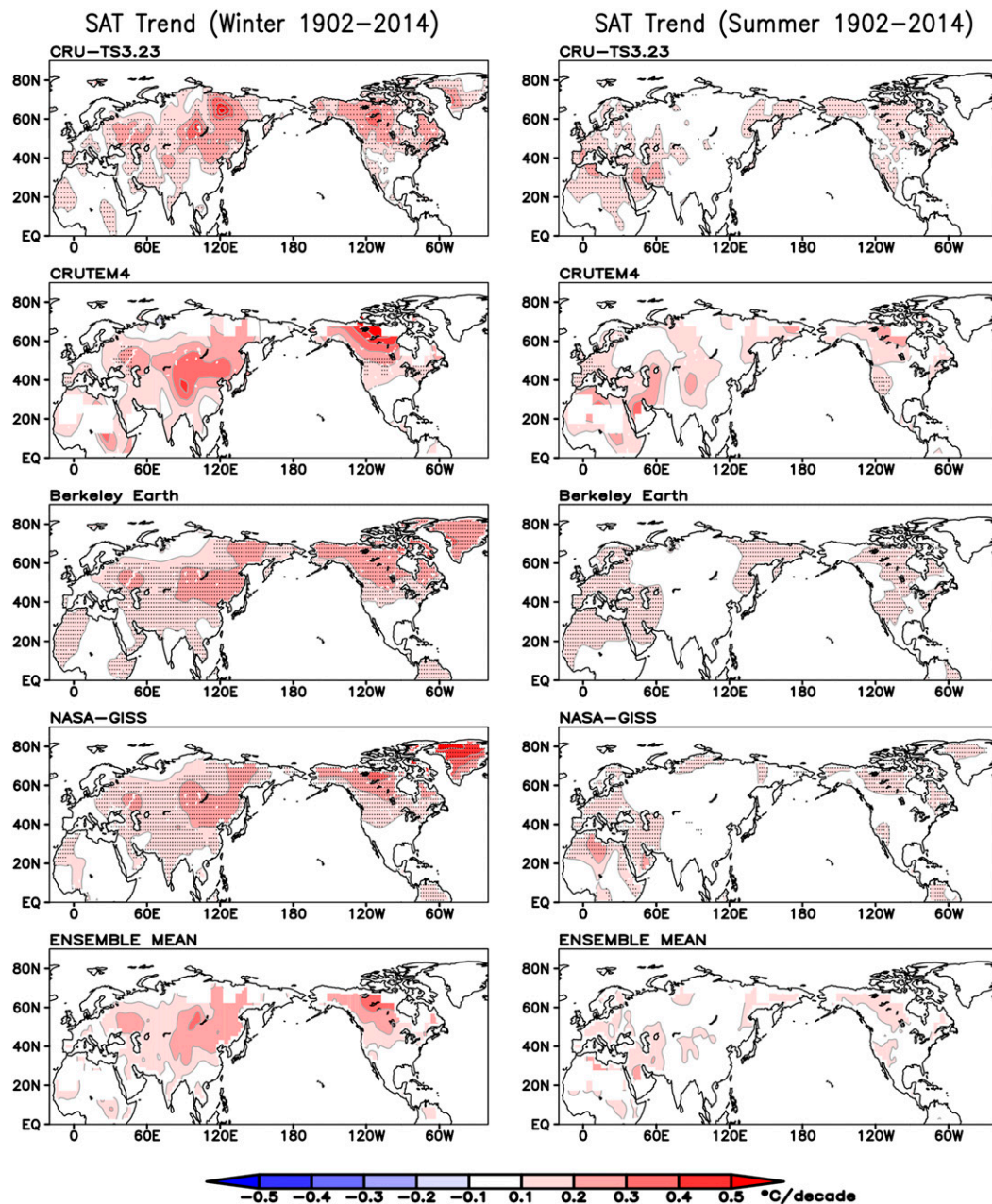


FIG. 2. The linear SAT trend in (left) winter (DJF) and (right) summer (JJA) during 1902–2014 in four observational analyses, and the average trend: (from top to bottom)  $0.5^\circ$  resolution CRU TS3.23,  $5.0^\circ$  resolution CRUTEM4;  $1.0^\circ$  resolution Berkeley Earth,  $2.0^\circ$  resolution NASA Goddard Institute for Space Studies (GISS) analysis, and the average of four linear trends (bottom), referred as the ensemble-mean trend. Contour interval and shading threshold is  $0.1^\circ\text{C decade}^{-1}$ , with warm colors showing a positive trend; all as before. The fields are displayed after 9, 1, 1, and 1 applications, respectively, of smth9. Trends significant at the 95% level are stippled.

indicates broad agreement over North America, eastern Europe, and Asia. The average trend from the four SAT analyses—the observation ensemble mean (Fig. 2, bottom panels)—confirms the striking seasonal variation of SAT trends over vast stretches of Asia and North America that were noted earlier.

#### 4. Surface air temperature trends in historical climate simulations

Historical simulations serve an important evaluative role for models whose projections of climate change constitute the backbone of the IPCC AR5 assessment

(Flato et al. 2013). The canonical evaluation from an intercomparison of the annual-mean warming trends is expanded upon here by analyzing the simulation of seasonal warming trends, an exercise seldom undertaken in the past. The ensemble mean of the century-long SAT trends in historical simulations generated by the five selected IPCC AR5 participant models is shown in Fig. 3, for both winter and summer. The winter SAT trend in the five historical simulations has varied, and often, unrealistic strength or structure (Fig. 3, left column): the GFDL-CM3 and UKMO HadCM3 and HadGEM2 simulations exhibit much weaker winter SAT trends (less than  $1.0^{\circ}\text{C century}^{-1}$ , the shading threshold) almost everywhere. On the other hand, the NCAR CCSM4 and MPI-ESM-LR simulations contain fairly realistic expressions of winter warming over Asia and North America. These simulations also exhibit weaker trends in summer, but not as weak as those observed.

#### a. Seasonal amplitude of SAT trends

The winter–summer difference, or the “seasonal amplitude” of SAT trends, is displayed in the right column of Fig. 3 using a lower contour interval to facilitate assessment of all five historical simulations. The observed amplitude (the target) is in the top panel, as before. The much weaker seasonality of SAT trends in the GFDL-CM3 and HadCM3 (and even HadGEM2-ES) historical simulations is now readily apparent, especially in the northern Great Plains and northwestern Canada. The amplitude of SAT trends is more realistic in the NCAR CCSM4 and MPI-ESM-LR simulations but the spatial structure is at some variance with the observed one. For example, these simulations exhibit large amplitude over North America in the region around Hudson Bay but the observed amplitude (top panel) is large southward of this region (i.e., just eastward of the Canadian Rockies). Over Asia, large amplitudes are focused on European Russia and Scandinavia in the simulations and over eastern Russia, Siberia, and Mongolia in observations.

#### b. Seasonal variation of regional SAT trends

The seasonal variation of SAT trends in two geographical regions exhibiting large winter warming in twentieth-century observations (regions 1 and 2 marked in the top-left panel of Fig. 3) is shown in Fig. 4. Over Alaska and western-central Canada (region 2), the observed SAT trend (thick solid black line) is largest in winter ( $\sim 2.5^{\circ}\text{C century}^{-1}$ ) and weakest in fall, when it is less than  $0.5^{\circ}\text{C century}^{-1}$ , or weaker by a factor of 4 compared to the winter value—a remarkable seasonal variation. In contrast, the multimodel ensemble-mean

SAT trend (thick dashed black line), obtained by averaging the trends in all historical simulations,<sup>1</sup> shows much weaker seasonal variability, weaker by at least a factor of 2. Of the constituent models, NCAR CCSM4 and the MPI-ESM-LR exhibit fairly realistic seasonal variations but for the increasing SAT trend in fall. The other three models generate weak SAT trends in all seasons, with the season of maximum (and minimum) trend at variance with observations. Over Mongolia and south-central Russia (region 1), the observed SAT trend is strongest in winter and weakest in summer; the winter-to-summer decline is by a factor of 4 or more, as before. In contrast, the multimodel ensemble-mean SAT trend is almost seasonally invariant.

The examined IPCC AR5 models are not viable investigative tools for analyzing the origin of the impressive seasonality in observed SAT trends in view of deficiencies in their representation of this feature; Stine et al. (2009) reached similar conclusions in the context of the IPCC AR4 models.

#### c. Intraensemble spread of winter SAT trends

The ensemble spread of the linear SAT trend in historical simulations from two IPCC AR5 climate system models—one from the United States (GFDL-CM3, with a 5-member ensemble) and the other from Europe (UKMO HadCM3, with a 9-member ensemble)—is displayed in Fig. 5a. The ensemble-averaged winter SAT trend is shown in the upper panels for the 1902–2004 (103 yr, referred to as century-long) and 1860–2004 (145 yr, referred to as century-plus) periods; linear trends in the two periods are compared to assess the impact of period length on linear trends. Although weaker linear trends were expected in the longer period from the more limited aliasing of low-frequency variability (of natural or anthropogenic origin), the century-long period was itself viewed as being long enough to accommodate (and average out) the decadal-to-multidecadal-scale low-frequency variability such as Pacific decadal variability (e.g., Mantua et al. 1997; Guan and Nigam 2008) and Atlantic multidecadal variability (e.g., Guan and Nigam 2009; Kavvada et al. 2013), two widely documented and analyzed decadal–multidecadal climate variabilities. As such, further weakening of the linear trend in the longer, century-plus period, notably in polar latitudes of the GFDL simulations, was somewhat unexpected, especially for the ensemble-averaged trend since ensemble averaging can additionally filter low-frequency variability assuming a

<sup>1</sup> 27 historical simulations from five models were analyzed, with each model (not each ensemble member) weighted equally.

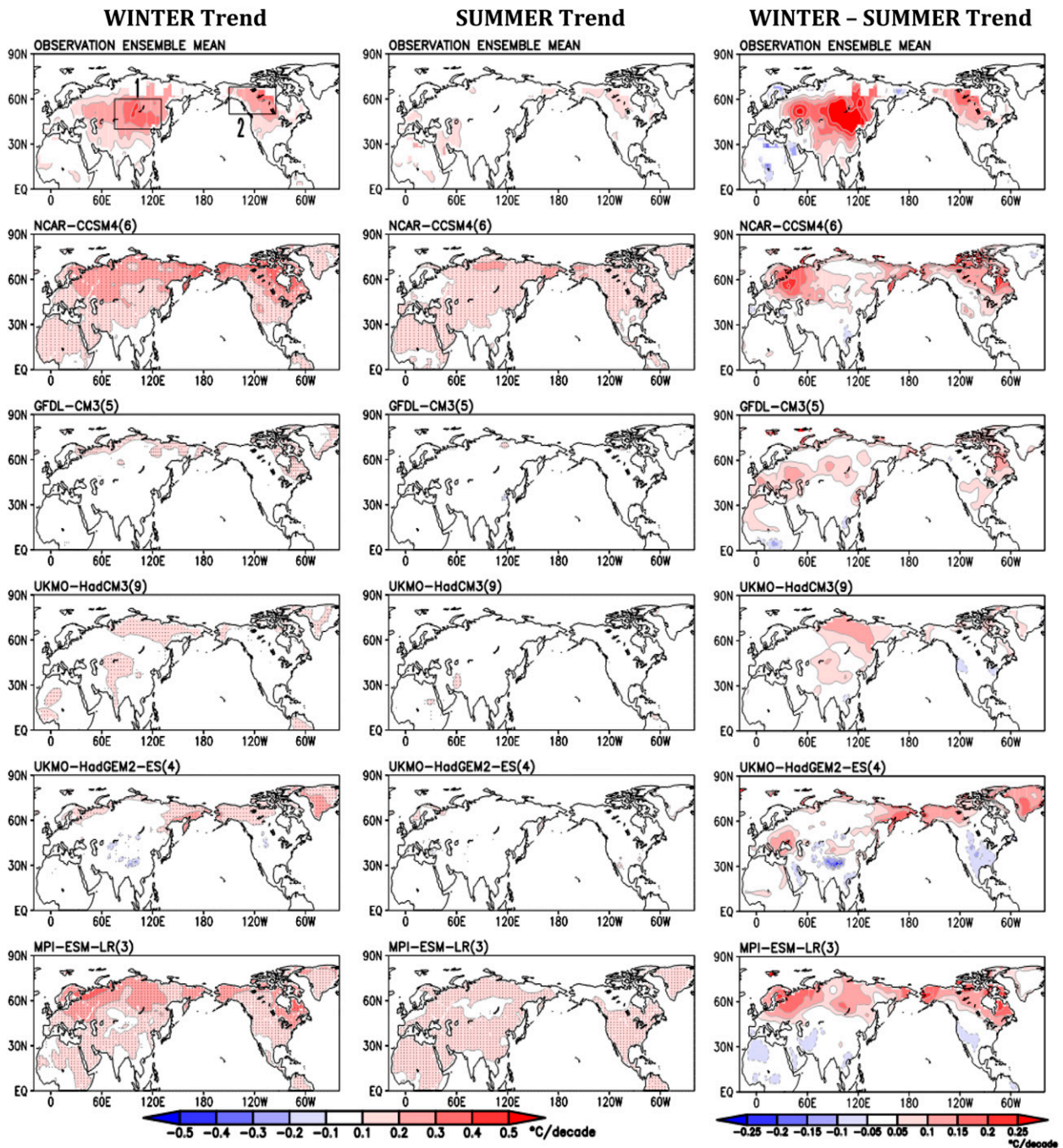


FIG. 3. The linear SAT trend in (left) winter (DJF) and (center) summer (JJA) in five IPCC-AR5 model simulations of twentieth-century climate (1902–2004). The seasonal amplitude in SAT trends, i.e., winter-minus-summer trends, are shown in the right column with half the interval used in the left ones. The number of ensemble members in each simulation is noted in parentheses, and the average trend across all ensemble members is shown. The average linear trend in the same period in four analyses of SAT observations (CRU-TS3.23, CRUTEM4, Berkeley Earth, and NASA-GISS; see text for details)—the observation ensemble and simulation target—is shown in the top row. As the model fields are on a relatively coarser grid (see data section), smth9 is applied only once on them. Shading and contouring are as in Fig. 1 for the left and center columns. Trends significant at the 95% level are stippled. The two regions exhibiting large winter trends in observations, Mongolia and south-central Russia including Lake Baikal (region 1) and Alaska and western-central Canada extending up to Hudson Bay (region 2), are marked in the top-left panel for later analysis.

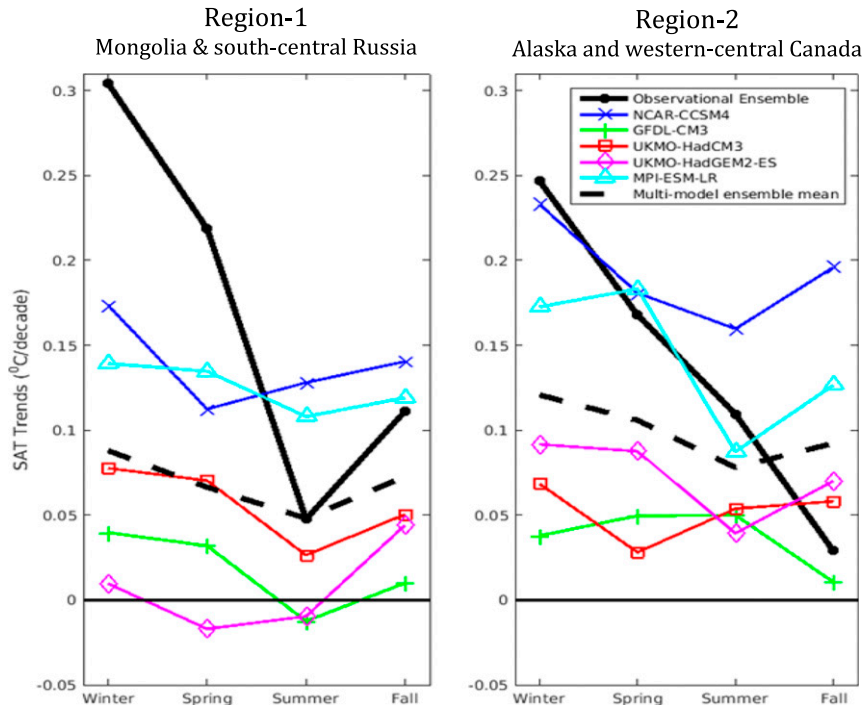


FIG. 4. The area-averaged seasonal SAT trends in region 1 (Mongolia and south-central Russia) and region 2 (Alaska and western-central Canada) for the 1902–2004 period; both regions are marked in Fig. 3 (top-left panel). The linear trend averaged across four observational analyses—the simulation target—is plotted using the thick black solid line, while the corresponding trend, averaged across all historical simulations (27 in number from 5 models), and referred to as the multimodel ensemble-mean trend, is shown by the thick black dashed line. The trends from individual models are shown using colored lines; see the legend.

sufficiently large ensemble size (e.g., Sardeshmukh et al. 2000). The corresponding trends in the HadCM3 simulations (Fig. 5a, right panels), in contrast, are relatively stable to the change in analysis period.

The intraensemble standard deviation (SD) of the century-long linear trend in the GFDL simulations is about twice as large as in HadCM3 simulations, especially over northern Eurasia, but the SD of the century-plus trend is quite comparable (Fig. 5a, lower panels). The impressive decline in the SD of the linear trend with increasing period length in the GFDL case indicates the presence of longer-than-centennial-scale low-frequency variability (or ultra-low-frequency variability) in its historical simulations, with related phase varying across ensemble members. The aliasing of this variability component into the century-long linear trend will depend on its phase in that century, but as all linear trends were computed for the same century (1902–2004), the ultra-low-frequency variability in the GFDL historical simulations is likely to be of “internal” origin (i.e., unforced).

The large intraensemble SD of the century-long linear SAT trend in the GFDL simulations, with the SD often

larger than the ensemble-averaged trend in the middle-to-high northern latitudes (i.e., the very regions exhibiting the strongest ensemble-averaged trend or potential secular warming) is concerning as the large SD is indicative of significant internal variability in the modeled climate. Is this unforced component of climate variability (“dynamical” noise) overwhelming the twentieth-century secular warming signal in the GFDL historical simulations?

The century-long (i.e., twentieth century) linear winter SAT trends in each ensemble member of the GFDL historical simulations are shown in Fig. 5b along with the ensemble-averaged trend (top panel) for easy reference. Of the five historical simulations, only run 2 yields quasi-realistic winter SAT trends. Interestingly, none of the simulations exhibit the pronounced winter warming trend over western-central Canada seen in observations (Figs. 1 and 2). It would be interesting to examine the amplitude and phase of ultra-low-frequency variability in run 2 (quasi-realistic trends), run 4 (largely devoid of trends), and run 5 (cooling trend over northwestern Eurasia).

The robustness of SAT trends in the models’ historical simulations is evaluated in appendix A.

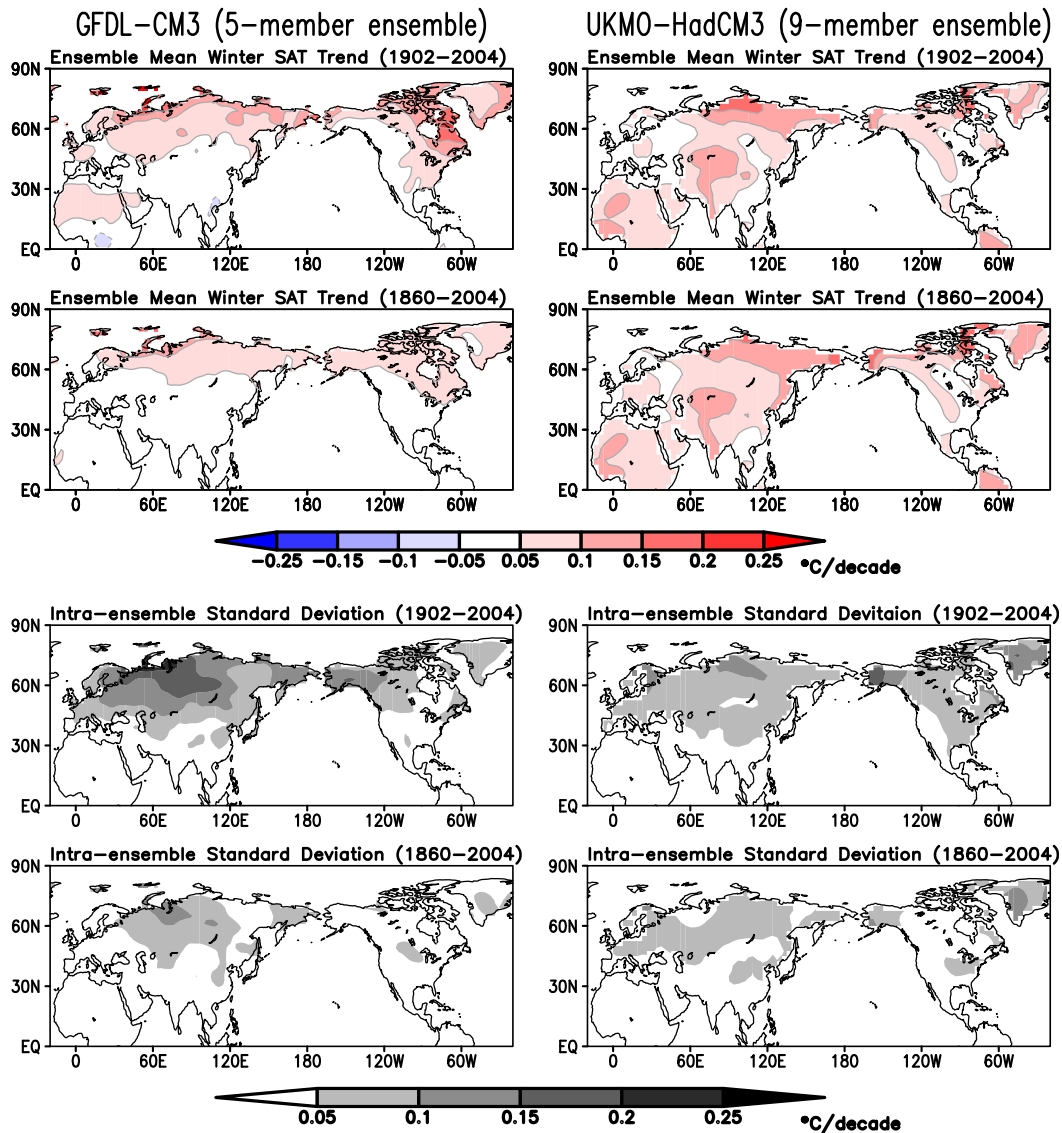


FIG. 5. (a) Ensemble mean and intraensemble spread of the winter SAT trend in the GFDL-CM3 and UKMO-HadCM3 historical climate simulations (a 5- and 9-member ensemble, respectively). Two periods are analyzed: the twentieth century (1902–2004) as before, and the longer 1860–2004 period spanning the nineteenth and twentieth centuries to reduce potential aliasing of multidecadal variability in linear trends. The ensemble-mean SAT trends for the two periods are shown in color while the intraensemble spread of SAT trends is shown in black and white, with the GFDL ones always on the left. A uniform contour interval of  $0.05^{\circ}\text{C decade}^{-1}$  is used in all panels, with contouring and shading threshold at  $0.05^{\circ}\text{C decade}^{-1}$ .

### 5. Origin of the striking seasonality in observed SAT trends

The large seasonality of SAT trends over the northern continents is intriguing. Clearly, it is not the reduced  $\text{CO}_2$  concentration in the agriculturally active summer season because this reduction, besides being small ( $\sim 10$  ppm or  $\sim 3\%$  of the average twentieth-century concentration), occurs each year, and thus cannot

account for the smaller *trend* in summer SAT. Surface albedo feedback from continental snow and ice cover also cannot account for the larger winter trends notwithstanding their high-latitude focus as this feedback is muted in winter because of diminished solar radiation. Although this feedback is robust in summer, it is incapable of generating a delayed warming over continents (unlike oceanic regions, where heat sequestration leads to larger surface warming in winter). There is no

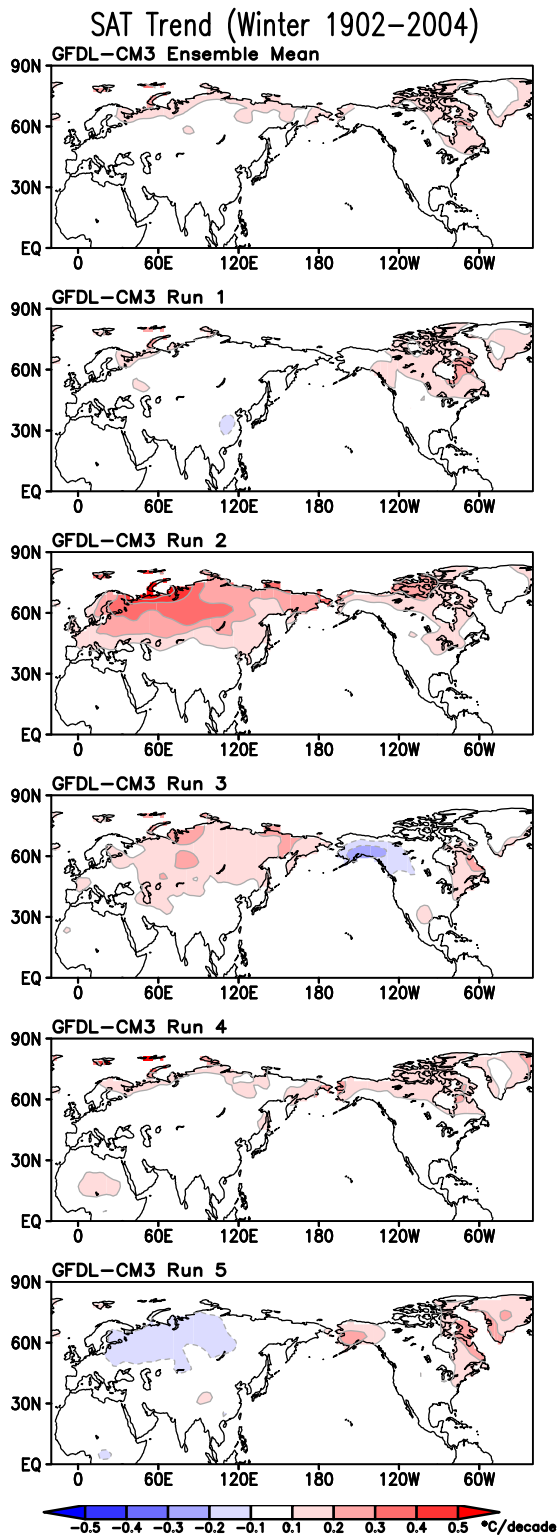


FIG. 5. (b) Ensemble spread in the century-long winter SAT trend in GFDL-CM3's historical simulations of twentieth-century climate. The five-member ensemble-mean trend, shown earlier in Fig. 5a, is displayed at the top for easy reference. Contouring and shading are as in Fig. 5a.

corresponding heat storage and delayed release mechanism operative over continental regions (Manabe and Stouffer 1980).

The mechanisms generating regional and seasonal variation of the century-long SAT trends have yet to be elucidated. Most previous attributions of the seasonality of warming are based on the change and/or trends over multidecadal periods, ranging from 36 years (Wallace et al. 2012) to 60 years (Stine and Huybers 2012). Because of the potential for aliasing low-frequency climate variability into multidecadal trends (as discussed in section 4) and the winter robustness of this variability (manifest in circulation footprints as well), related thermal advection is implicated in the generation of stronger SAT trends over northern continents in boreal winter (Wang et al. 2009; Stine et al. 2009; Wallace et al. 2012; Stine and Huybers 2012). Multidecadal SAT trends have been attributed also to humidity advection (by the same low-level circulation anomalies) and ensuing radiative impacts (e.g., Compo and Sardeshmukh 2009).

Two mechanisms for the striking seasonality in observed SAT trends are discussed: A new mechanism rooted in land surface–hydroclimate interactions is proposed in section 5a and a dynamical mechanism based on thermal advection by the secular change in circulation in section 5b.

#### a. Land surface–hydroclimate interaction mechanism

A mechanism grounded in land surface–hydroclimate interactions is proposed for the large seasonality in SAT trends over the northern continents. In a column perspective, the change in the downward longwave radiative flux at Earth's surface from increased greenhouse gas concentrations—estimated at  $\sim 7 \text{ W m}^{-2} \text{ per } ^\circ\text{C}$  of annual-mean warming from the IPCC AR5 models (Stephens et al. 2012)—must be offset, with the offsetting processes determining the new equilibrium surface air temperature. In winter when the hydrologic cycle over the northern continents is dormant (from a frozen land surface), this excess incident energy would have to be offset, primarily, by increased surface longwave emission (i.e., by raising surface temperature); any offsets by increased upward sensible heat flux would also entail raising surface temperature. If the same amount of excess longwave radiation was incident in summer, it could be disposed of, additionally, by increased continental evapotranspiration and snowmelt, that is, without raising the surface temperature as much as in winter. If this were the case, a larger secular trend in summer evapotranspiration, and late-spring and fall snowmelt, should be found in regions exhibiting large seasonality in SAT trends (Fig. 3, top-right panel). Of the two, longer historical records are available for

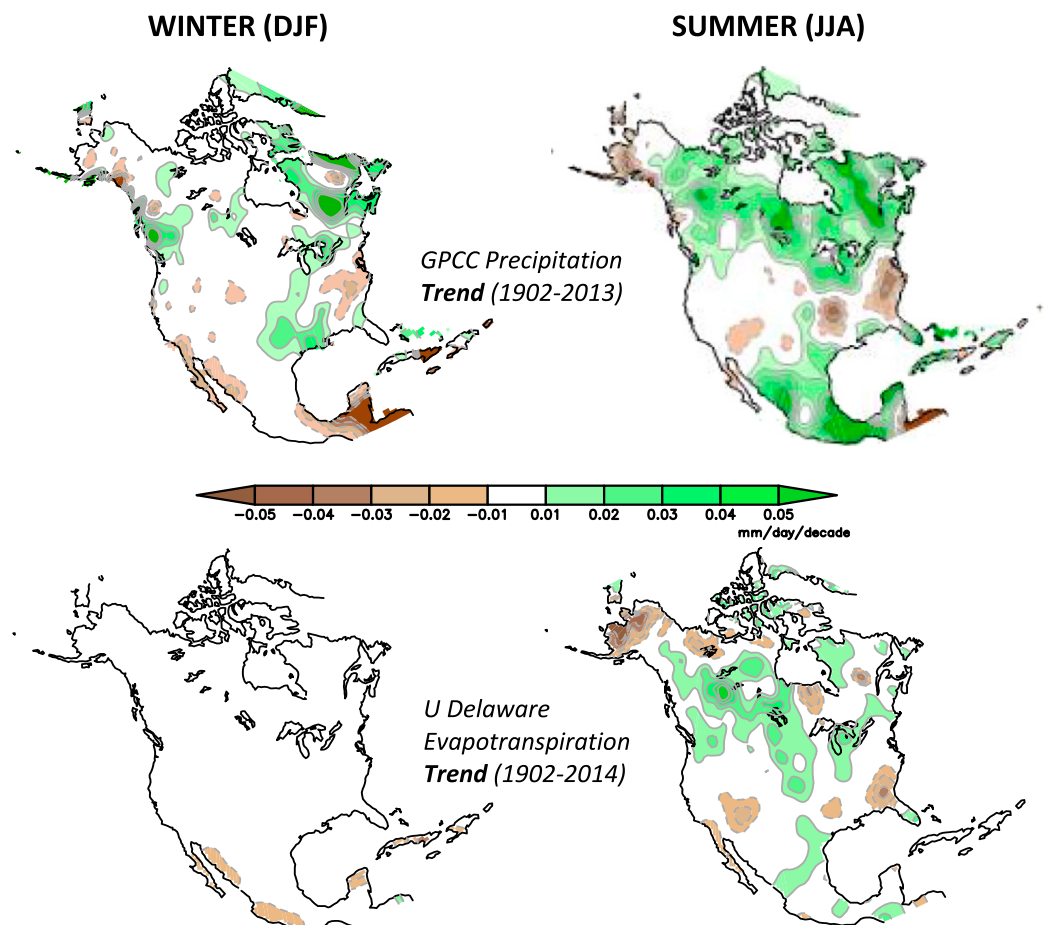


FIG. 6. (a) Linear trends in winter and summer in (top) GPCP precipitation and (bottom) University of Delaware evapotranspiration in  $\text{mm day}^{-1} \text{decade}^{-1}$ , using common shading and contour. All fields are shown after nine applications of smth9 in GrADS.

evapotranspiration (1902–2014); snow cover extent records begin only in the mid-1960s (Estilow et al. 2015) and snowmelt records remain unavailable, precluding their use in this preliminary investigation of the large seasonality in century-long SAT trends. Although evapotranspiration estimates are available since the early twentieth century, the diagnosis of evapotranspiration is not without some uncertainties (Nigam and Ruiz-Barradas 2006). For these reasons, trends in precipitation—a directly measured/monitored quantity—are examined first. Figure 6a indeed shows larger century-long precipitation trends in summer over some of the pertinent North American regions. However, as the regional atmospheric water cycle also involves moisture transports (Nigam and Ruiz-Barradas 2006), the larger summer precipitation trends noted above are not necessarily indicative of increasing regional evapotranspiration but certainly encouraging of further analysis.

The century-long (1902–2014) winter and summer evapotranspiration trends from the University of

Delaware diagnosis (Willmott et al. 1985) are shown in the lower panels of Fig. 6a, and the summer-minus-winter difference in Fig. 6b in green/brown. The differences are large over western-central Canada and the northern-central Great Plains, notably the southern Mackenzie Plain (i.e., southward of Great Slave Lake and westward of Lake Athabasca), the Canadian Shield, and the northern Great Plains—interestingly, the very regions where the seasonal difference in SAT trends is large. To facilitate recognition of the extent of overlap of the regions exhibiting large seasonality in the evapotranspiration and SAT trends, the winter-minus-summer SAT trends<sup>2</sup> are overlaid in red in Fig. 6b. The extent of

<sup>2</sup> SAT trends here are from the CRU-TS3.23 data and for the same period as the evapotranspiration ones (1902–2014), also the period used in Fig. 1. This period is 10 yr longer than the one used in Fig. 3.

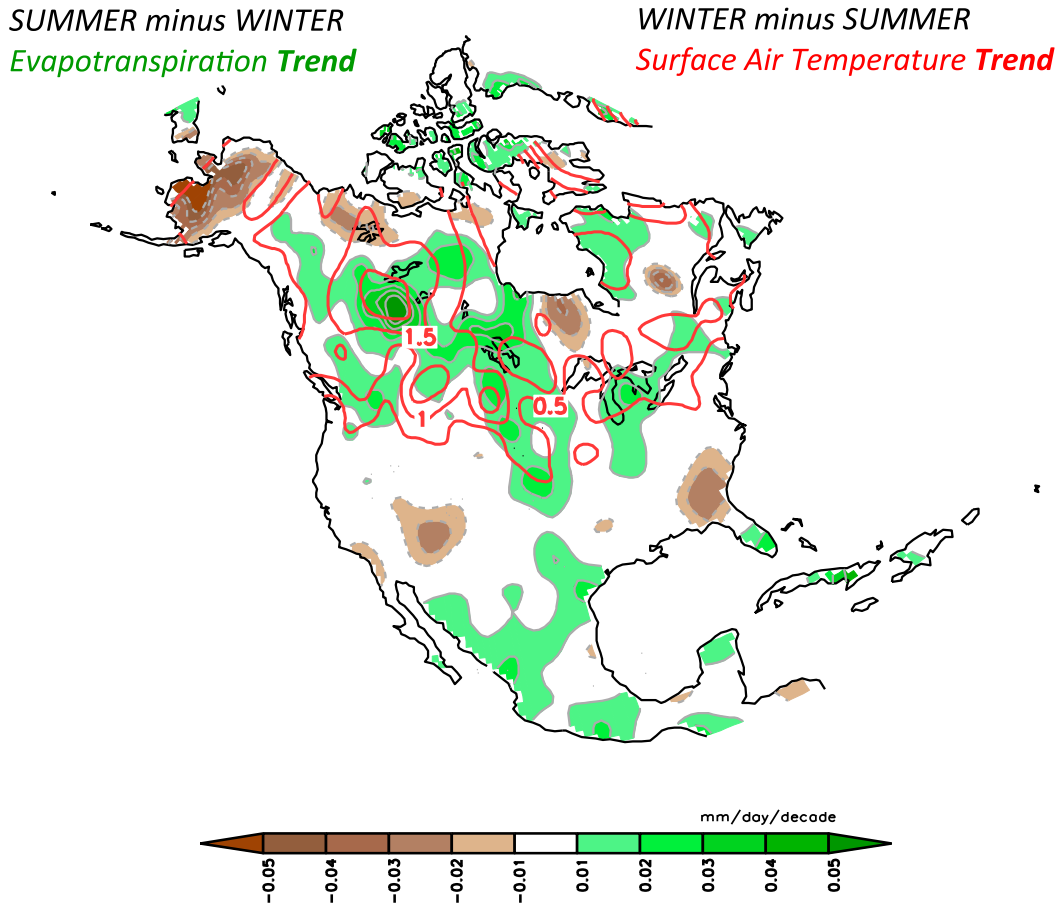


FIG. 6. (b) Summer-minus-winter evapotranspiration trends (shaded green/brown) with overlaid winter-minus-summer surface air temperature trends (contoured in red) for the same 1902–2014 period. Note the opposite seasonal differencing of the two trends. Evapotranspiration is from the University of Delaware while the surface air temperature is from the CRU TS3.23 dataset and contoured with an interval of  $0.5^{\circ}\text{C century}^{-1}$ . All fields are shown after nine applications of smth9 in GrADS.

geographical overlap is impressive,<sup>3</sup> and promising for the attribution of the winter–summer differences in century-long SAT trends to land surface–hydroclimate interactions permitted by the seasonal hydrologic state of the middle- to high-latitude continents.

#### DISCUSSION

The proposed mechanism is energetically viable: The average summer-minus-winter evapotranspiration trend in the overlap regions of Fig. 6b (bottom

panel) is estimated to be  $\sim 0.175 \text{ mm day}^{-1} \text{ century}^{-1}$ , a value in between the second and third green contours. The energy needed for fueling additional evapotranspiration in summer is estimated as  $(0.175 \times 10^{-3}) \{ \text{m day}^{-1} \text{ century}^{-1} \} \times 1000 \{ \text{kg m}^{-3} \} \times L_c \{ \text{J kg}^{-1} \}$ , where curly brackets note the dimensional units of the preceding quantities and  $L_c$  is the latent heat of condensation ( $2.5 \times 10^6$ ), yielding  $4.375 \times 10^5 \text{ J m}^{-2} \text{ day}^{-1} \text{ century}^{-1}$  or  $\sim 5.0 \text{ W m}^{-2} \text{ century}^{-1}$ .

Is this latent energy consumption energetically consistent with the summer reduction in SAT trends (by  $\sim 1.25^{\circ}\text{C century}^{-1}$  in the overlap regions)? The complexity of the climate system and the absence of extended records of surface energy flux measurements preclude an observationally rooted answer. We thus seek the assistance of climate models, notwithstanding their imperfections (cf. Fig. 3), in relating surface energy consumption/deposition with SAT trends. The IPCC AR5 models indicate a  $\sim 7 \text{ W m}^{-2}$  increase in downward

<sup>3</sup>The broad overlap of red contours with the green shaded region in western-central Canada is apparent and impressive. Although spatial correlation, which quantitatively measures the correspondence of field departures from their regional average (i.e., of more granular structures), is not a suitable measure of regional-scale overlap, note that it is 0.33 for region 2 (marked in Fig. 3, top-left panel), for reference.

surface longwave radiative flux for every  $1^{\circ}\text{C century}^{-1}$  of warming (Stephens et al. 2012). Using this measure, albeit for global and annual-mean model responses, a  $1.25^{\circ}\text{C century}^{-1}$  reduction of winter SAT trend (to bring it down to the summer value) will require latent disposition of  $\sim 8.75 \text{ W m}^{-2} \text{ century}^{-1}$ , that is, more than the  $\sim 5.0 \text{ W m}^{-2} \text{ century}^{-1}$  estimated from the observed winter-to-summer increase in evapotranspiration trends. Interestingly, this discrepancy, especially the larger winter-to-summer latent disposition estimate, was anticipated because the winter warming has been attributed both to radiative and dynamical effects but with the dynamical contribution deemed insufficient in accounting for the seasonal differences in SAT trend over the northern continents (Stine et al. 2009). Without the dynamical contribution, which is significant only in winter, the winter-minus-summer SAT trend would be smaller, leading to a smaller winter-to-summer latent disposition requirement—one more in line with the  $\sim 5.0 \text{ W m}^{-2} \text{ century}^{-1}$  estimate developed from seasonal differences in evapotranspiration trends.

The winter dormancy of the continental hydrologic cycle is central to the proposed mechanism. The correspondence between the seasonal differences in SAT and evapotranspiration trends is thus sought only over the middle- to high-latitude continents where the winter dormancy condition is met. As such, the lack of overlap of the trend differences over the southern tier states, Mexico, and Central America in Fig. 6b does not undermine the proposed mechanism.

The strikingly different seasonal states of the hydrologic cycle over the middle- to high-latitude continents—winter dormancy and summer vigor—can impart a pronounced seasonality to the secular warming of these continental regions, as indicated by this analysis of the century-long observational datasets. Clearly, this mechanism needs corroboration,<sup>4</sup> in addition to the evaluation of other impacts on long-term SAT trends (e.g., from the cloud cover, specific humidity, snow cover extent, snowmelt, and permafrost variations and trends). It also raises interesting questions—Is the increasing summer evapotranspiration over northern North America during the twentieth century (cf. Fig. 6a) a reflection of the greening of the boreal forests from increasing  $\text{CO}_2$  concentration and warming temperatures (e.g., Myneni et al. 1997; Piao et al. 2006)? Would positive evapotranspiration trends be present even in the absence of the  $\text{CO}_2$  fertilization of boreal forests? Controlled experiments with climate

system models could provide insight into the mechanisms once these models begin to portray the pronounced seasonality of the century-long SAT trends seen in nature.

### b. Dynamical contribution to the century-long SAT trends

The dynamical contribution to secular warming refers to the warming component arising from circulation change rather than radiative forcing (e.g., Wallace et al. 2012). Most previous estimates of this contribution are based on analyses of the changes/trends over multidecadal periods ranging from 36 to 60 years<sup>5</sup> and, as such, are prone to the aliasing of low-frequency climate variability into multidecadal trends. The dynamical contribution to multidecadal SAT trends is, in part, rooted in this aliasing, and its seasonal sensitivity rooted in the winter robustness of low-frequency variability and related thermal advection.<sup>6</sup> The contribution is positive for warm advection (i.e., when the low-level circulation anomalies are from southward latitudes or adjoining oceans). The impact of the low-level circulation anomalies on SAT trends is often referred as the dynamical contribution (see footnote 6).

The attribution of the seasonality in century-long trends should be more straightforward, in part, from the reduced aliasing of low-frequency variability into centennial trends. The 113-yr period analyzed here is longer than the known periods of low-frequency climate variability (subdecadal to multidecadal), limiting potential aliasing.<sup>7</sup> The dynamical contribution to the

<sup>5</sup> Compo and Sardeshmukh (2009) analyze change during 1961–2006; Wang et al. (2009) investigate model trends during 1951–2000; Stine et al. (2009) focus on the 1954–2007 trends; Stine and Huybers (2012) target the 1951–2010 period; Wallace et al. (2012) analyze trends over a 36-yr period (1965–2000).

<sup>6</sup> Thermal advection anomaly =  $-\mathbf{V}_{\text{LF Var}} \cdot \nabla T_{\text{Clim}} - \mathbf{V}_{\text{LF Var}} \cdot \nabla T_{\text{LF Var}} - \mathbf{V}_{\text{Clim}} \cdot \nabla T_{\text{LF Var}}$ , where  $\mathbf{V}_{\text{LF Var}}$  and  $T_{\text{LF Var}}$  are the low-frequency variability related low-level wind and temperature anomaly, and  $\mathbf{V}_{\text{Clim}}$  and  $T_{\text{Clim}}$  the climatological low-level wind and temperature. This first and third terms are linear in anomaly while the second (self-advection) is nonlinear and, often, much smaller than the other two. Interestingly,  $T_{\text{LF Var}}$  can be reasonably reconstructed from thermal advection during winter variability episodes (e.g., Baxter and Nigam 2015). The essentially linear thermal advection is thus a surrogate for  $T_{\text{LF Var}}$ , with the first term being a clear dynamical contribution to the temperature anomaly. The same cannot be said for the second and third terms, especially if diabatic heating (e.g., radiative forcing in context of secular warming) is also contributing in generation of the temperature anomaly  $T_{\text{LF Var}}$ .

<sup>7</sup> Ideally, the period for trend analysis should be a few multiples of the longest variability time scale to preclude its aliasing.

<sup>4</sup> Two independent diagnoses of evapotranspiration are compared in appendix B.

century-long SAT trends could, however, still be significant, not from continued aliasing but from the secular trends in seasonal circulation—the basis for dynamical contribution in this analysis.

The dynamical contribution to multidecadal (1965–2000) SAT trends was evaluated by Wallace et al. (2012), who used regressions of monthly sea level pressure on the hemispheric-averaged (40°–90°N) continental winter SAT to identify the influential SLP pattern. Projections of monthly SLP on this pattern generated an SLP index, which was then regressed out of SAT, with the deficit revealing the dynamical contribution. This strategy was not adopted here for the following reasons:

- The influential SLP pattern cannot be a surrogate for just the dynamical contribution as it must include a component from the secular warming of the planetary boundary layer (V. Ravi et al. 2017, unpublished manuscript), that is, a thermal part reflecting hydrostatic balance. Removing this SLP pattern's entire influence from SAT is an overkill. [Targeting SLP gradients, i.e., circulation directly, would have been preferable.]
- The SLP pattern, obtained from contemporaneous regressions (Wallace et al. 2012), cannot be entirely viewed as a “predictor” of the dynamical influence on concurrent SAT.
- The century-long SAT trends exhibit coherent, regional structures (Fig. 1); extensive spatial averaging (e.g., hemispheric) can thus weaken the contribution of regional thermal advection.

The dynamical contribution is assessed here by focusing directly on the SLP trend, from whose gradients the geostrophic wind trend ( $\mathbf{V}_{g\_trend}$  in units of  $\text{m s}^{-1} \text{decade}^{-1}$ ) is inferred. The climatological SLP from the HadSLP2 dataset (Allan and Ansell 2006) with its prominent winter features—the Siberian high (>1028 hPa), Aleutian low (<1008 hPa), and Icelandic low (<1006 hPa)—is displayed in Fig. 7a (top panel), along with the century-long trends (shaded). The SLP trends exhibit coherent regional structure, suggesting a slight northeastward shift of the Aleutian low in view of the 1–2 hPa drop-off of SLP over Alaska and the Yukon Territory, and modest weakening of the Icelandic low by 2–3 hPa over the twentieth century; in contrast, SLP trends are weak over Europe and Asia. The structure of the twentieth-century SLP trends in the Western Hemisphere indicates a southeasterly geostrophic wind trend over northern North America, with the exception of Alaska and the Yukon Territory, where the wind trends are northwesterly to westerly.

The SLP trends are much weaker in spring and summer over northwest North America (Fig. 7a), a region exhibiting notable seasonal differences in century-long SAT trends (the red contoured region in Fig. 6b, or top-right panel in Fig. 3). The weakness of SLP trends and, more importantly, their horizontal gradients in spring and summer indicate the relative insignificance of the dynamical contribution to SAT trends in these seasons. This too is interesting as it provides a discriminating seasonal phase space for resolving the contributions of land surface–hydroclimate interactions and dynamical advection in seasonal secular warming over northern North America.

The dynamical contribution to the seasonality of secular warming over North America ( $T_{L\_dyn}$ ) is shown in Fig. 7b with red-blue contours. The contribution to the winter-minus-summer SAT trends is distributed widely over the continent; that is, it extends well beyond the northern half where the seasonality of century-long SAT trends is concentrated (red contoured region in Fig. 6b) and where the winter–summer difference of evapotranspiration trends is also focused (green/browns in Fig. 7b or 6b). Interestingly, the dynamical component often complements the evapotranspiration one over the northern continent, as indicated by the structure of the two contributions in Fig. 7b:

- Focusing on the prominent feature of the dynamical contribution—the warming extending southwestward from the Nunavut Territory into Saskatchewan and Montana, with a prominent center over the Reindeer Lake (Fig. 7b)—one notes the weakness of the evapotranspiration contribution around Reindeer Lake and over northern Nunavut, the regions where it was unable to account for the observed seasonality of SAT trends ( $\sim 1^\circ\text{C century}^{-1}$ , cf. Fig. 6b). The complementary dynamical contribution remedies this accounting deficit.
- Focusing now on the prominent feature of the evapotranspiration contribution—the regional maximum centered on the southern Mackenzie Plain (i.e., southward of Great Slave Lake and westward of Lake Athabasca; Fig. 7b)—one notes the weakness of the dynamical contribution, especially over the southwestern Mackenzie Plain where this contribution is not only weak but also offsets the evapotranspiration contribution. In this region, where the seasonality of SAT trends is strongest ( $\sim 2^\circ\text{C century}^{-1}$ ; cf. Fig. 6b), the dynamical contribution is insignificant and the evapotranspiration one dominant. Farther to the south, however (i.e., over southwestern Saskatchewan and northern Montana), the two contributions become comparable.

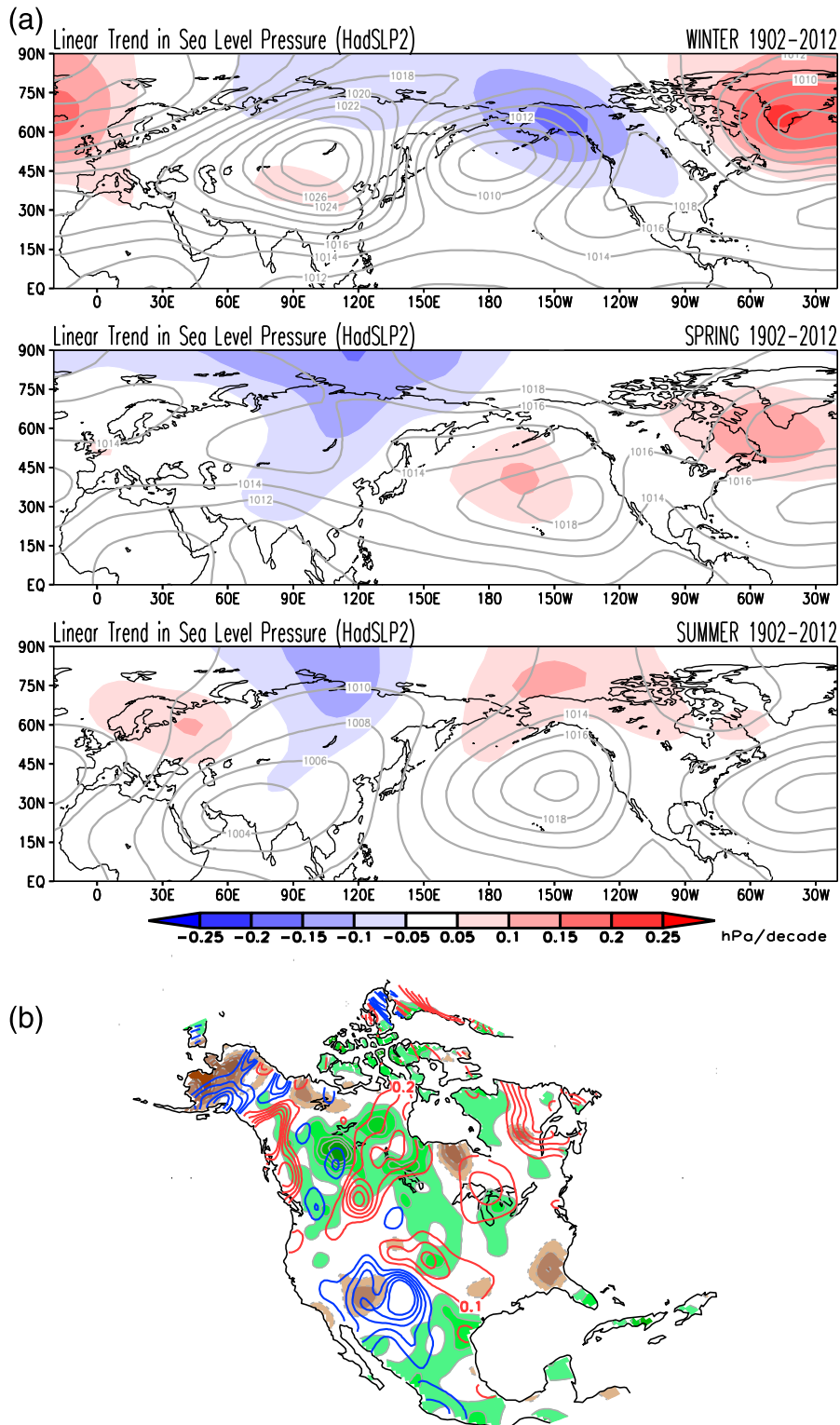


FIG. 7. (a) Seasonal sea level pressure (SLP) and SLP trend in the Northern Hemisphere. The climatological (1902–2012) SLP is contoured with a 2.0-hPa interval, while the SLP trend is shaded with an interval of 0.05 hPa decade<sup>-1</sup>. The HadSLP2 data are analyzed and plotted after nine applications of the nine-point smoother (smth9) in GrADS. (b) The dynamical contribution to the 1902–2012 winter-minus-summer SAT trend is shown in red (positive) and blue (negative) contours, with an interval of 0.1°C decade<sup>-1</sup>. It is superposed on the evapotranspiration contribution (shaded green/brown, exactly as in Fig. 6b) to recognize regions of complementary and supplementary contributions.

## 6. Concluding remarks

Secular warming of the northern continents is a well-studied topic as it typically involves computation of the linear trend—an elemental mathematical operation—on the near-surface air temperature (SAT) record, a meteorological variable measured with varying degrees of precision since the eighteenth century. The twentieth-century linear trend in annual SAT is a widely used marker of secular warming, and its sensitivity to SAT analysis, analysis period, and computation methodology (e.g., minimization of least squares or absolute distance) have all been assessed in numerous studies.

Somewhat less studied is the striking seasonality of the observed twentieth-century SAT trends, the focus of this analysis. Why is this easily characterized seasonality of interest? To begin with, the large seasonal variation of climate over the Northern Continents provides multiple base states for the expression of secular warming. The resulting seasonal variation in century-long SAT trends—shown to be remarkable, especially over North America and central-eastern Asia—can provide rare insights into the dynamical and thermodynamical processes generating secular warming over the land surface. No less important is the exceptional opportunity provided by this seasonality—an expanded climate phase space—for vetting climate projection models without additional model integrations, a cost-effective evaluative opportunity that remains largely untapped.

The urgent need for shifting the evaluative and diagnostic focus away from the customary *annual mean* toward the *seasonal cycle* of secular warming is manifest in the *inability* of the leading climate models (whose simulations inform the IPCC's Fifth Assessment Report) to generate realistic and robust (large signal-to-noise ratio) twentieth-century winter and summer SAT trends over the northern continents. The large intra-ensemble SD of century-long SAT trends in some IPCC AR5 models (e.g., GFDL-CM3) moreover raises interesting questions: If this subset of climate models is realistic, especially in generation of ultra-low-frequency variability, is the century-long (1902–2014) linear trend in observed SAT—a one-member ensemble of the climate record—a reliable indicator of the secular warming signal? Can the shorter recent period (1970–2014) exhibiting even larger linear SAT trends be reasonably referred to as the “accelerated warming” period, given the potential for increased aliasing of the multidecadal and ultra-low-frequency variability components into the 45-yr linear trend?

Two mechanisms for the large seasonality of the century-long SAT trends over the northern continents

are investigated, including a new one based on land surface–hydroclimate interactions.

The new mechanism posits the relative weakness of the summer trends to the “awakened” hydrologic state in summer, following winter–spring dormancy. An active hydrologic cycle brings into play land surface processes that can potentially offset the additional longwave radiation incident on the land surface from increasing greenhouse gas concentrations. Whereas the offset is primarily from increased surface longwave emission in winter (thereby raising surface air temperature), observational evidence is presented for latent disposal in summer through increased evapotranspiration (i.e., without necessarily raising surface temperature); this disposal mechanism is, of course, not available in winter when the hydrologic cycle is dormant. An estimate of the power needed to fuel the observed positive trend in summer evapotranspiration was, moreover, shown to be in accord with estimates of the additional longwave radiative energy incident on Earth's surface from increasing greenhouse gas concentrations. The land surface–hydroclimate interaction mechanism merits closer scrutiny from analysis of additional observational and simulation datasets.

The seasonality of SAT trends was hitherto attributed to the warming component generated by circulation variability and change (the dynamical contribution) rather than to greenhouse radiative forcing (e.g., Wallace et al. 1995, 2012); the contribution is seasonally sensitive in view of the winter robustness of low-frequency variability and related thermal advection. Most previous assessments of the dynamical contribution were, however, in the context of multidecadal (and not century-long) SAT trends and, as such, impacted by aliasing of low-frequency variability. The dynamical contribution, calculated here, from century-long trends in low-level circulation, was found to be relatively modest and, interestingly, often complementary to the evapotranspiration contribution.

The spring-to-summer reduction in the century-long SAT trends over North America (Fig. 1), that is, across two seasons exhibiting insignificant SLP trends over the continent (Fig. 7a), reiterates the limited reach of the dynamical mechanism in generating the seasonality in SAT trends. Additional evidence for the primacy of the land surface–hydroclimate interaction mechanism is the finding from analysis of radiosonde data [the National Climatic Data Center's Radiosonde Atmospheric Temperature Products for Assessing Climate B (RATPAC-B) dataset] that the seasonal amplitude of century-long SAT trends is largest at the surface and diminishes with height in the lower troposphere; that is, it is

surface trapped (V. Ravi et al. 2017, unpublished manuscript).

The relative contribution of both mechanisms to the observed seasonality in century-long SAT trends needs further assessment because of uncertainties in the diagnosis of evapotranspiration and sea level pressure from the century-long observational records. Climate system models—ideal tools for investigation of mechanisms through controlled experimentation—are unfortunately not yet ready given their inability to simulate the seasonality of trends in historical simulations.

**Acknowledgments.** The authors (SN, NPT, and ARB) would like to acknowledge the support of the National Science Foundation, through NSF Grant AGS1439940 to the University of Maryland. Natalie Thomas' doctoral studies are partially supported by Scott Weaver's Presidential Early Career Award for Scientists and Engineers (PECASE 2012) funds routed to University of Maryland, and by the Department of Defense, Air Force Office of Scientific Research, National Defense Science and Engineering Graduate Fellowship, 32 CFR 168a (2015-2018). NPT performed the analysis and developed figures as part of her doctoral research; ARB helped with data set development, statistical analysis, and graphics; SJW provided feedback on the interim analysis, and SN conceived and directed the project, and developed the manuscript with NPT's assistance. The authors thank Editor Anthony Broccoli and the two reviewers for their careful reading and helpful advice in improving the manuscript.

## APPENDIX A

### Robustness of Century-Long SAT Trends in IPCC-AR5 Historical Simulations

The robustness of *winter* SAT trends is evaluated by dividing the ensemble-averaged trend (the signal) by the intraensemble standard deviation of the century-long trends (the noise); the signal-to-noise ratio is shown in Fig. A1. The heavier shading (smaller ratios) identifies the subregions where the indicated secular winter warming is, in fact, not robust on account of the large regional “dynamical” noise in historical simulations. As the ensemble size varies considerably (from 3 to 9), intermodel comparisons of the shaded regions are not appropriate. The GFDL and NCAR models, however, have similar ensemble size (5 and 6, respectively) but pronouncedly different ratios: Over northern Asia, dynamical noise overwhelms the secular warming signal in the GFDL-CM3 historical

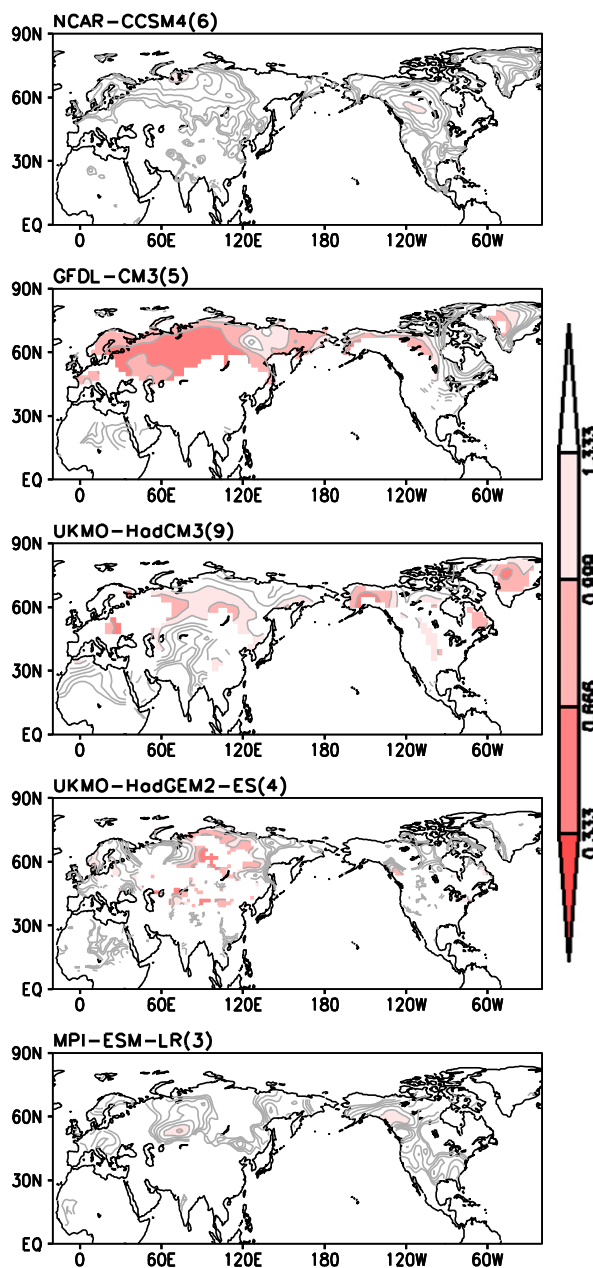


FIG. A1. Ratio of the ensemble-averaged winter SAT trend to the intraensemble standard deviation of the winter trend. The ratio is plotted only where the ensemble-averaged winter trend is  $\geq 0.5^{\circ}\text{C century}^{-1}$ , i.e., only in the model-indicated secular warming regions. The linear trend over the 1902–2004 period is computed in all cases. The contour interval is 0.333, with values  $\leq 1.333$  shaded and heavier shading for smaller values. Smaller values (more reds) denote regions where the ensemble-mean SAT trend is less robust. Smoothing is as in Fig. 3.

simulations but not in the NCAR-CCSM4 ones. The signal-to-noise ratio is larger than 1.333 almost everywhere in the NCAR simulations, as it is in the MPI-ESM-LR ones.

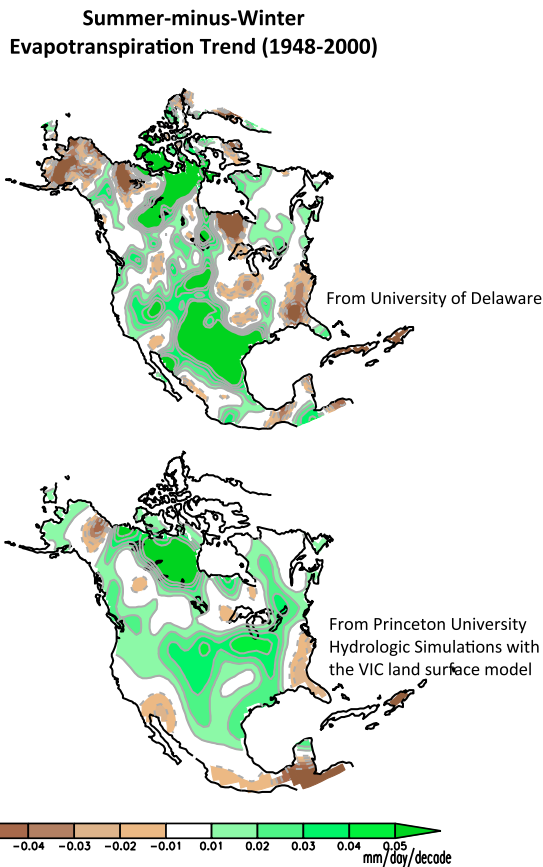


FIG. B1. Intercomparison of the winter-minus-summer evapotranspiration trends from two independent evapotranspiration diagnoses, in their common period (1948–2000). Data from the University of Delaware’s Terrestrial Water Budget Archive (V.3.01, Willmott et al. 1985) are used in the top panel, and from Princeton University’s Global Land Surface Hydrology Simulations with the VIC land surface model (Sheffield and Wood 2007) in the bottom panel. The common shading and contouring, as per shading bar.

The analysis suggests some caution in the use of unweighted multimodel ensemble-average for characterization and attribution of secular warming.

## APPENDIX B

### Diagnoses of Evapotranspiration

Given the central role of evapotranspiration in the proposed land surface–hydroclimate interaction mechanism and the challenging nature of its diagnosis, a recent independent estimate from Princeton University’s Global Land Surface Hydrology Simulations with the VIC land surface model (Sheffield and Wood 2007) is intercompared with the University of Delaware’s diagnosis. The recent VIC model based evapotranspiration

was not part of the main analysis as it is available only for the second half of the twentieth century (1948–2000). The summer-minus-winter evapotranspiration trends from both datasets are shown for this common period in Fig. B1. There are regional differences to be sure, but they are embedded in a broadly similar pattern that includes larger values over the Northwest Territories in Canada and over the central and southern Great Plains. The similarity over Northwest Territories and the surrounding regions is somewhat reassuring.

## REFERENCES

- Abatzoglou, J. T., and K. T. Redmond, 2007: Asymmetry between trends in spring and autumn temperature and circulation regimes over western North America. *Geophys. Res. Lett.*, **34**, L18808, doi:10.1029/2007GL030891.
- , D. E. Rupp, and P. W. Mote, 2014: Seasonal climate variability and change in the Pacific Northwest of the United States. *J. Climate*, **27**, 2125–2142, doi:10.1175/JCLI-D-13-00218.1.
- Allan, R., and T. Ansell, 2006: A new globally complete monthly historical gridded mean sea level pressure dataset (HadSLP2): 1850–2004. *J. Climate*, **19**, 5816–5842, doi:10.1175/JCLI3937.1.
- Balling, R. C., Jr., P. J. Michaels, and P. C. Knappenberger, 1998: Analysis of winter and summer warming rates in gridded temperature time series. *Climate Res.*, **9**, 175–181, doi:10.3354/cr009175.
- Bauer, P., A. Thorpe, and G. Brunet, 2015: The quiet revolution of numerical weather prediction. *Nature*, **525**, 47–55, doi:10.1038/nature14956.
- Baxter, S., and S. Nigam, 2015: Key role of the North Pacific Oscillation–west Pacific pattern in generating the extreme 2013/14 North American winter. *J. Climate*, **28**, 8109–8117, doi:10.1175/JCLI-D-14-00726.1.
- Becker, A., and Coauthors, 2013: A description of the global land-surface precipitation data products of the Global Precipitation Climatology Centre with sample applications including centennial (trend) analysis from 1901–present. *Earth Syst. Sci. Data*, **5**, 71–99, doi:10.5194/essd-5-71-2013.
- Brutsaert, W., 2006: Indications of increasing land surface evaporation during the second half of the 20th century. *Geophys. Res. Lett.*, **33**, L20403, doi:10.1029/2006GL027532.
- Compo, G. P., and P. D. Sardeshmukh, 2009: Oceanic influences on recent continental warming. *Climate Dyn.*, **32**, 333–342, doi:10.1007/s00382-008-0448-9.
- Dima, I. M., and J. M. Wallace, 2003: On the seasonality of the Hadley cell. *J. Atmos. Sci.*, **60**, 1522–1527, doi:10.1175/1520-0469(2003)060<1522:OTSOTH>2.0.CO;2.
- Dwyer, J. G., M. Biasutti, and A. H. Sobel, 2012: Projected changes in the seasonal cycle of surface temperature. *J. Climate*, **25**, 6359–6374, doi:10.1175/JCLI-D-11-00741.1.
- Estilow, T. W., A. H. Young, and D. A. Robinson, 2015: A long-term Northern Hemisphere snow cover extent data record for climate studies and monitoring. *Earth Syst. Sci. Data*, **7**, 137–142, doi:10.5194/essd-7-137-2015.
- Flato, G., and Coauthors, 2013: Evaluation of climate models. *Climate Change 2013: The Physical Science Basis*, T. F. Stocker et al., Cambridge University Press, 741–866.
- Fyfe, J. C., N. P. Gillett, and D. W. J. Thompson, 2010: Comparing variability and trends in observed and modelled global-mean

- surface temperature. *Geophys. Res. Lett.*, **37**, L16802, doi:10.1029/2010GL044255.
- Guan, B., and S. Nigam, 2008: Pacific sea surface temperatures in the twentieth century: An evolution-centric analysis of variability and trend. *J. Climate*, **21**, 2790–2809, doi:10.1175/2007JCLI2076.1.
- , and —, 2009: Analysis of Atlantic SST variability factoring interbasin links and the secular trend: Clarified structure of the Atlantic multidecadal oscillation. *J. Climate*, **22**, 4228–4240, doi:10.1175/2009JCLI2921.1.
- Hansen, J., R. Ruedy, M. Sato, and K. Lo, 2010: Global surface temperature change. *Rev. Geophys.*, **48**, RG4004, doi:10.1029/2010RG000345.
- Harris, I., P. D. Jones, T. J. Osborn, and D. H. Lister, 2014: Updated high-resolution grids of monthly climatic observations—The CRU TS3.10 dataset. *Int. J. Climatol.*, **34**, 623–642, doi:10.1002/joc.3711.
- Hegerl, G. C., J. von Storch, K. Hasselmann, B. D. Santer, U. Cubasch, and P. D. Jones, 1996: Detecting greenhouse-gas-induced climate change with an optimal fingerprint method. *J. Climate*, **9**, 2281–2306, doi:10.1175/1520-0442(1996)009<2281: DGGICC>2.0.CO;2.
- Hoskins, B. J., 1996: On the existence and strength of the summer subtropical anticyclones. *Bull. Amer. Meteor. Soc.*, **77**, 1287–1291.
- Jones, P. D., D. H. Lister, T. J. Osborn, C. Harpham, M. Salmon, and C. P. Morice, 2012: Hemispheric and large-scale land surface air temperature variations: An extensive revision and an update to 2010. *J. Geophys. Res.*, **117**, D05127, doi:10.1029/2011JD017139.
- Kavvada, A., A. Ruiz-Barradas, and S. Nigam, 2013: AMO's structure and climate footprint in observations and IPCC AR5 climate simulations. *Climate Dyn.*, **41**, 1345–1364, doi:10.1007/s00382-013-1712-1.
- Kusunoki, S., T. Nakaegawa, and O. Arakawa, 2009: Simulations of land-surface air temperature and land precipitation in the twentieth century by the MJ98 AGCM. *J. Meteor. Soc. Japan*, **87**, 473–495, doi:10.2151/jmsj.87.473.
- Lau, N.-C., 1979: The observed structure of tropospheric stationary waves and the local balances of vorticity and heat. *J. Atmos. Sci.*, **36**, 996–1016, doi:10.1175/1520-0469(1979)036<0996: TOSOTS>2.0.CO;2.
- Lindzen, R. S., and A. V. Hou, 1988: Hadley circulations for zonally averaged heating centered off the equator. *J. Atmos. Sci.*, **45**, 2416–2427, doi:10.1175/1520-0469(1988)045<2416: HCFZAH>2.0.CO;2.
- Lu, J., and M. Cai, 2009: Seasonality of polar surface warming amplification in climate simulations. *Geophys. Res. Lett.*, **36**, L16704, doi:10.1029/2009GL040133.
- Manabe, S., and R. J. Stouffer, 1980: Sensitivity of a global climate model to an increase of CO<sub>2</sub> concentration in the atmosphere. *J. Geophys. Res.*, **85**, 5529–5554, doi:10.1029/JC085iC10p05529.
- Mantua, N., S. Hare, Y. Zhang, J. Wallace, and R. Francis, 1997: A Pacific interdecadal climate oscillation with impacts on salmon production. *Bull. Amer. Meteor. Soc.*, **78**, 1069–1079, doi:10.1175/1520-0477(1997)078<1069: APICOW>2.0.CO;2.
- Matsuura, K., and C. J. Willmott, 2015: Terrestrial precipitation: 1900–2014 gridded monthly time series. University of Delaware Dept. of Geography. [Available online at [http://climate.geog.udel.edu/~climate/html\\_pages/Global2014/README\\_GlobalTsP2014.html](http://climate.geog.udel.edu/~climate/html_pages/Global2014/README_GlobalTsP2014.html).]
- Meehl, G. A., and Coauthors, 2007: Global climate projections. *Climate Change 2007: The Physical Science Basis*, S. Solomon et al., Eds., Cambridge University Press, 747–845.
- , and Coauthors, 2014: Decadal climate prediction: An update from the trenches. *Bull. Amer. Meteor. Soc.*, **95**, 243–267, doi:10.1175/BAMS-D-12-00241.1.
- Mitchell, T. P., and J. M. Wallace, 1992: The annual cycle in equatorial convection and sea surface temperature. *J. Climate*, **5**, 1140–1156, doi:10.1175/1520-0442(1992)005<1140: TACIEC>2.0.CO;2.
- Mote, P., 2003: Trends in temperature and precipitation in the Pacific Northwest during the twentieth century. *Northwest Sci.*, **77**, 271–282.
- Murphy, J. M., D. M. H. Sexton, D. N. Barnett, G. S. Jones, M. J. Webb, M. Collins, and D. A. Stainforth, 2004: Quantification of modelling uncertainties in a large ensemble of climate change simulations. *Nature*, **430**, 768–772, doi:10.1038/nature02771.
- Myneni, R. B., C. D. Keeling, C. J. Tucker, G. Asrar, and R. R. Nemani, 1997: Increased plant growth in the northern high latitudes from 1981 to 1991. *Nature*, **386**, 698–702, doi:10.1038/386698a0.
- NCAR, 2014: The climate data guide: Precipitation data sets: Overview and comparison table. [Available online at <https://climatedataguide.ucar.edu/climate-data/precipitation-datasets-overview-comparison-table>.]
- Nigam, S., and Y. Chao, 1996: Evolution dynamics of tropical ocean-atmosphere annual cycle variability. *J. Climate*, **9**, 3187–3205, doi:10.1175/1520-0442(1996)009<3187: EDOTOA>2.0.CO;2.
- , and A. Ruiz-Barradas, 2006: Seasonal hydroclimate variability over North America in global and regional reanalyses and AMIP simulations: Varied representation. *J. Climate*, **19**, 815–837, doi:10.1175/JCLI3635.1.
- , and S. C. Chan, 2009: On the summertime strengthening of the Northern Hemisphere Pacific sea level pressure anticyclone. *J. Climate*, **22**, 1174–1192, doi:10.1175/2008JCLI2322.1.
- Oort, A. H., and J. J. Yienger, 1996: Observed interannual variability in the Hadley circulation and its connection to ENSO. *J. Climate*, **9**, 2751–2767, doi:10.1175/1520-0442(1996)009<2751: OIVITH>2.0.CO;2.
- Philander, S. G. H., and Y. Chao, 1991: On the contrast between the seasonal cycles of the equatorial Atlantic and Pacific Oceans. *J. Phys. Oceanogr.*, **21**, 1399–1406, doi:10.1175/1520-0485(1991)021<1399: OTCBTS>2.0.CO;2.
- Piao, S., P. Friedlingstein, P. Ciais, L. Zhou, and A. Chen, 2006: Effect of climate and CO<sub>2</sub> changes on the greening of the Northern Hemisphere over the past two decades. *Geophys. Res. Lett.*, **33**, L23402, doi:10.1029/2006GL028205.
- Rasmusson, E. M., 1968: Atmospheric water vapor transport and the water balance of North America. II: Large-scale water balance investigations. *Mon. Wea. Rev.*, **96**, 720–734, doi:10.1175/1520-0493(1968)096<0720: AWWTAT>2.0.CO;2.
- Redmond, K. T., and J. T. Abatzoglou, 2014: Current climate and recent trends. *Climate Change in North America*, G. Ohring, Ed., Springer, 53–94.
- Rhode, R., and Coauthors, 2013: Berkeley Earth temperature averaging process. *Geoinf. Geostat. Overview*, **1**, 1000103, doi:10.4172/2327-4581.1000103.
- Robeson, S. M., C. J. Willmott, and P. D. Jones, 2014: Trends in hemispheric warm and cold anomalies. *Geophys. Res. Lett.*, **41**, 9065–9071, doi:10.1002/2014GL062323.
- Ruiz-Barradas, A., and S. Nigam, 2005: Warm-season rainfall variability over the U.S. Great Plains in observations, NCEP and ERA-40 reanalyses, and NCAR and NASA atmospheric model simulations. *J. Climate*, **18**, 1808–1830, doi:10.1175/JCLI3343.1.
- Santer, B. D., T. M. L. Wigley, J. S. Boyle, D. J. Gaffen, J. J. Hnilo, D. Nychka, D. E. Parker, and K. E. Taylor, 2000: Statistical

- significance of trends and trend differences in layer-averaged atmospheric temperature time series. *J. Geophys. Res.*, **105**, 7337–7356, doi:[10.1029/1999JD901105](https://doi.org/10.1029/1999JD901105).
- Sardeshmukh, P. D., G. P. Compo, and C. Penland, 2000: Changes of probability associated with El Niño. *J. Climate*, **13**, 4268–4286, doi:[10.1175/1520-0442\(2000\)013<4268:COPAWE>2.0.CO;2](https://doi.org/10.1175/1520-0442(2000)013<4268:COPAWE>2.0.CO;2).
- Sheffield, J., and E. F. Wood, 2007: Characteristics of global and regional drought, 1950–2000: Analysis of soil moisture data from off-line simulation of the terrestrial hydrologic cycle. *J. Geophys. Res.*, **112**, D17115, doi:[10.1029/2006JD008288](https://doi.org/10.1029/2006JD008288).
- , G. Goteti, and E. F. Wood, 2006: Development of a 50-yr high-resolution global dataset of meteorological forcings for land surface modeling. *J. Climate*, **19**, 3088–3111, doi:[10.1175/JCLI3790.1](https://doi.org/10.1175/JCLI3790.1).
- Stephens, G. L., and Coauthors, 2012: An update on Earth's energy balance in light of the latest global observations. *Nat. Geosci.*, **5**, 691–696, doi:[10.1038/ngeo1580](https://doi.org/10.1038/ngeo1580).
- Stine, A. R., and P. Huybers, 2012: Changes in the seasonal cycle of temperature and atmospheric circulation. *J. Climate*, **25**, 7362–7380, doi:[10.1175/JCLI-D-11-00470.1](https://doi.org/10.1175/JCLI-D-11-00470.1).
- , —, and I. Y. Fung, 2009: Changes in the phase of the annual cycle of surface temperature. *Nature*, **457**, 435–441, doi:[10.1038/nature07675](https://doi.org/10.1038/nature07675).
- Taylor, K. E., R. J. Stouffer, and G. A. Meehl, 2012: An overview of CMIP5 and the experiment design. *Bull. Amer. Meteor. Soc.*, **93**, 485–498, doi:[10.1175/BAMS-D-11-00094.1](https://doi.org/10.1175/BAMS-D-11-00094.1).
- Thompson, D. W. J., J. M. Wallace, P. D. Jones, and J. J. Kennedy, 2009: Identifying signatures of natural climate variability in time series of global-mean surface temperature: Methodology and insights. *J. Climate*, **22**, 6120–6141, doi:[10.1175/2009JCLI3089.1](https://doi.org/10.1175/2009JCLI3089.1).
- Trenberth, K. E., and Coauthors, 2007: Observations: Surface and atmospheric climate change. *Climate Change 2007: The Physical Science Basis*, S. Solomon et al., Eds., Cambridge University Press, 235–336.
- Wallace, J. M., Y. Zhang, and J. A. Renwick, 1995: Dynamic contribution to hemispheric mean temperature trends. *Science*, **270**, 780–783, doi:[10.1126/science.270.5237.780](https://doi.org/10.1126/science.270.5237.780).
- , Q. Fu, B. V. Smoliak, P. Lin, and C. M. Johanson, 2012: Simulated versus observed patterns of warming over the extratropical Northern Hemisphere continents during the cold season. *Proc. Natl. Acad. Sci. USA*, **109**, 14 337–14 342, doi:[10.1073/pnas.1204875109](https://doi.org/10.1073/pnas.1204875109).
- Wang, H., S. Schubert, M. Suarez, J. Chen, M. Hoerling, A. Kumar, and P. Pegion, 2009: Attribution of the seasonality and regionality in climate trends over the United States during 1950–2000. *J. Climate*, **22**, 2571–2590, doi:[10.1175/2008JCLI2359.1](https://doi.org/10.1175/2008JCLI2359.1).
- Willmott, C. J., C. M. Rowe, and Y. Mintz, 1985: Climatology of the terrestrial seasonal water cycle. *J. Climatol.*, **5**, 589–606, doi:[10.1002/joc.3370050602](https://doi.org/10.1002/joc.3370050602).